

Metals in the Intracluster Medium of MS 1512.4+3647 Observed with Suzaku: Implications for the Metal Enrichment History

Yuya SHIMODA,¹ Madoka KAWAHARADA,² Kosuke SATO,³ Takaya OHASHI,⁴ Yoshitaka ISHISAKI,⁴ Ikuyuki MITSUISHI,⁴
Hiroki AKAMATSU,⁵ and Makoto S. TASHIRO¹

¹*Department of Physics, Saitama University, 255 Shimo-Okubo, Sakura, Saitama 338-8570
shimoda@heal.phy.saitama-u.ac.jp*

²*Institute of Space and Astronautical Science, JAXA, 3-1-1 Yoshinodai, Chuo-ku, Sagami-hara, Kanagawa 252-5210*

³*Department of Physics, Tokyo University of Science, 1-3 Kagurazaka, Shinjuku-ku, Tokyo 162-8601*

⁴*Department of Physics, Tokyo Metropolitan University, 1-1 Minami-Osawa, Hachioji, Tokyo 192-0397*

⁵*SRON Netherlands Institute for Space Research, Sorbonnelaan 2, 3584, CA, Utrecht, The Netherlands*

(Received 2012 November 26; accepted 2013 July 17)

Abstract

The cluster of galaxies MS 1512.4+3647 ($z = 0.372$) was observed with Suzaku for 270 ks. Besides the Fe abundance, the abundances of Mg, Si, S, and Ni are separately determined for the first time in a medium redshift cluster ($z > 0.3$). The derived abundance pattern of MS 1512.4+3647 is consistent with those of nearby clusters, suggesting that the system has similar contributions from supernovae (SNe) Ia and SNe II to nearby clusters. The number ratio of SNe II to SNe Ia is ~ 3 . The estimated total numbers of both SNe II and SNe Ia against gas mass indicate similar correlation with those for the nearby clusters. The abundance results of MS 1512.4+3647 is consistent with the standard scenario that the SN II rate history roughly follows the star-formation history which has a peak at $1 < z < 2$ and then declines by about one order of magnitude toward $z \sim 0$. The similar number of SNe Ia to the nearby clusters suggests that the SN Ia rate declines steeply from $z = 0.37$ to $z = 0$ and/or SN Ia explosions occurred predominantly at larger redshifts.

Key words: galaxies: clusters: individual (MS 1512.4+3647) – X-rays: galaxies: clusters – X-rays: ICM

1. Introduction

Clusters of galaxies are the largest virialized structures in the universe, and they gravitationally bind hot thin-thermal plasma (intracluster medium; ICM). The high temperature reaching up to several 10^7 K make the ICM to produce X-rays via thermal bremsstrahlung. The ICM is enriched with metals having been synthesized in stars and supernova (SN) explosions and ejected to the intra-galactic space by SN explosions (e.g. Arnaud et al. 1992; Renzini et al. 1993). The metals in galaxies are thought to be exported to the ICM via galaxy wind (Mathews & Baker 1971) and/or ram pressure stripping (Gunn & Gott 1972). These metals are highly ionized in collisional ionization equilibrium and excited metal ions emit atomic lines in the X-ray range.

The majority of supernovae are classified into type Ia (SN Ia) and type II (SN II). The former is the explosion of a white dwarf with gas accretion from a companion star, in which nuclides are in the thermal equilibrium and provides a lot of iron family elements (Iwamoto et al. 1999). On the other hand, in the latter the iron core of a massive star are photodisintegrated into helium nuclei and mainly alpha elements are synthesized in the explosion (Nomoto et al. 2006). Thus the emission lines observed in the X-ray spectrum reflect integrated activities of both types of supernovae in the galaxies, and enable us to study chemical

enrichment history of the ICM, which is a major component of the known baryon in the universe.

Observational studies of metals in the ICM were greatly advanced by ASCA. In particular, it allowed to measure spatial distributions of Si and Fe in the ICM (Fukazawa et al. 1998, 2000; Finoguenov et al. 2000, 2001; Ezawa et al. 1997). Recently, XMM-Newton and Chandra, thanks to their large effective areas and high angular resolutions, have measured “metal abundance” of the ICM in high-redshift clusters, which is a representative abundance for various elements, mainly determined by using Fe-L and Fe-K lines. Using XMM-Newton and Chandra data of 56 clusters at $0.3 \leq z \leq 1.3$, Balestra et al. (2007) measured the iron abundance Z_{Fe} within a spatial region of $0.15 r_{200} - 0.3 r_{200}$. They found that the clusters at $z > 0.5$ have a constant average abundance $Z_{\text{Fe}} \approx 0.25$ solar, while clusters at $z < 0.5$ exhibit a significantly larger abundance of $Z_{\text{Fe}} \approx 0.4$ solar. Maughan et al. (2008) also reported the same result using 115 clusters at $0.1 < z < 1.3$ observed with Chandra. They found significant evolution in the metal abundance which drops by 50% from $z = 0.1$ to $z \sim 1$. Anderson et al. (2009) found the similar drop in the metal abundance from $z = 0.1$ to $z \sim 1$ using 29 clusters observed with XMM-Newton, together with the 115 clusters of Maughan et al. (2008) and 70 clusters at $z < 0.3$ in Snowden et al. (2008). Baldi et al. (2012) tried to study dependence of the metal evolution on distance

from the center by spatially resolved analysis, but they obtained no statistically significant conclusion about the different evolutionary path that the different regions of the clusters may have traversed.

After the launch of Suzaku (Mitsuda et al. 2007), studies of alpha elements have made progress. X-ray Imaging Spectrometer (XIS: Koyama et al. 2007) onboard Suzaku has good sensitivity for lines in lower energies thanks to good line spread function and low particle background level, especially in the earlier phases after launch for the less contamination affected the effective area in lower energies (Koyama et al. 2007). The metal abundances synthesized mainly in SNe II, such as O and Mg, in the ICM outside cool-core regions up to $\sim 0.3r_{200}$ have been measured for several nearby clusters and groups ($z \sim 0.001$) with Suzaku (Matsushita et al. 2007; Komiyama et al. 2009; Sato et al. 2007a, 2008, 2009a, 2010; Sakuma et al. 2011). Combining the Suzaku results with SNe nucleosynthesis model, Sato et al. (2007b) calculated integrated numbers of SNe Ia and SNe II explosions in nearby clusters. They showed that the number ratio of SNe II to Ia is ~ 3.5 and Fe has been synthesized predominantly by SNe Ia. A similar result is reported in de Plaa et al. (2007) using data of XMM-Newton.

In order to conclude the metal enrichment history of the ICM observationally, it is crucial to measure metal abundances of individual elements in clusters at high redshifts. This is beyond the ability of X-ray observatories currently in orbit, and would be one of major sciences in future X-ray missions with huge effective areas. However, Suzaku has the ability to pilot that survey for bright sources at medium redshifts.

We selected a target for Suzaku to perform the study of chemical evolution in the ICM. The criteria for the cluster are 1) distant but bright enough, 2) metal rich, and 3) cool (below 4 keV). In general, a luminous cluster has high temperature. However, in the high temperature gas, most alpha elements are fully ionized and hence no (or very weak) emission lines are expected. This is why we set the third criterion. As a result, we chose MS 1512.4+3647 at $z = 0.372$ (Stoche et al. 1991). Using ASCA data of MS 1512.4+3647, Ota (2000) reported its flux of 3.9×10^{-13} erg s $^{-1}$ cm $^{-2}$ in 2.0–10.0 keV, luminosity of $3.6_{-0.2}^{+0.2} \times 10^{44}$ erg s $^{-1}$, metal abundance of $1.05_{-0.67}^{+1.34}$ solar (Anders and Grevesse 1989) and temperature of $2.85_{-0.49}^{+0.91}$ keV. In this paper, we report results of our Suzaku long observation of the cluster of galaxies MS 1512.4+3647. Throughout this paper, cosmological parameters of $H_0 = 71$ km s $^{-1}$ Mpc $^{-1}$, $\Omega_M = 0.27$, and $\Omega_\Lambda = 0.73$ are adopted. At $z = 0.372$, 1' corresponds to 306 kpc. The virial radius of MS 1512.4+3647 is $r_{200} = 1.22$ Mpc by substituting the average temperature 2.85 keV (Ota 2000) into equation 2 of Henry et al. (2009), where $r_{200} = 1.22$ Mpc is the radius within which the average density is 200 times the critical density at the redshift of the cluster. The Galactic hydrogen column density in the direction of MS 1512.4+3647 is $N_H = 1.4 \times 10^{20}$ cm $^{-2}$ (Dickey & Lockman 1990). The definition of one solar

abundance is taken from Lodders (2003). Errors are given at the 90 % confidence level unless otherwise stated.

2. Observation and Data Reduction

2.1. Suzaku Observation

A Suzaku observation of MS 1512.4+3647 was performed from 2007 December 29 15:37:13 UT to 2008 January 4 16:40:18 UT with the total exposure of 268.9 ks (ObsID 802034010). In this paper, we utilize only the XIS data, since no signals are observed by the HXD. Two front-illuminated (FI: XIS0 and XIS3) CCD cameras and one back-illuminated (BI: XIS1) CCD camera were in operation. The average pointing direction of the XIS was at $(\alpha, \delta) = (15^{\text{h}}14^{\text{m}}25^{\text{s}}.4, +36^{\circ}37'11''.3)$. All the three XIS detectors were in the normal clocking mode (8 s exposure per frame) with the standard 5×5 and 3×3 editing modes during the data rates of SH/H and M/L, respectively.

We reprocessed unscreened XIS event files using Suzaku software version 19 in HEASoft 6.12 while referring to the calibration data base (CALDB) of the XIS and the X-ray telescope (XRT: Serlemitsos et al. 2007) released on 2012 February 10 and 2011 June 30, respectively. The `aepipeline` tool in the HEASoft package was used for the reprocessing. We applied the standard screening criteria for good time intervals (GTI): the spacecraft is outside the South Atlantic Anomaly (SAA), the time interval after an exit from the SAA is longer than 436 s, the geomagnetic cutoff rigidity (COR) is higher than 8 GV, the source elevation above the rim of bright and night Earth (ELV) is higher than 20° and 5° , respectively, and the XIS data are free from telemetry saturation. We selected XIS events with the ASCA grades of 0, 2, 3, 4, or 6. These procedures yielded an effective exposure of 208.6 ks. The resulting summed image of XIS0, XIS1, and XIS3 in the 0.5–7.0 keV energy range is shown in panel (a) of figure 1. The spectral analysis was performed with XSPEC 12.7.1.

2.2. Archival Chandra Data

MS 1512.4+3647 was observed with Chandra (Weisskopf et al. 2000, 2002) for 49.6 ks in 2000 (ObsID 800). The observation separated into two intervals, from 2000 June 6 15:53:46 UT to June 7 02:49:17 UT (hereafter OBS1), and from 2000 July 7 05:17:39 UT to July 7 09:25:15 UT (hereafter OBS2). We utilized this Chandra data to make ancillary response files (ARFs) of Suzaku and extract point sources. Chips S1, S2, S3, S4, I2 and I3 were used in the Advanced CCD Imaging Spectrometer (ACIS; Bautz et al. 1998; Garmire et al. 2003).

All the data were reprocessed with `chandra_repro` software to create new level 2 event files for the two intervals using CIAO 4.3 software package, referring to CALDB 4.4.6.1. The effective exposure became 36.4 ks for OBS1 and 12.6 ks for OBS2. In the following analysis, the same grade selection as that for the Suzaku XIS data (i.e., 0, 2, 3, 4, or 6) was applied. The resulting ACIS image in the 0.5–7.0 keV energy range is shown in panel (b) of figure 1 with the field of view (FOV) of XIS.

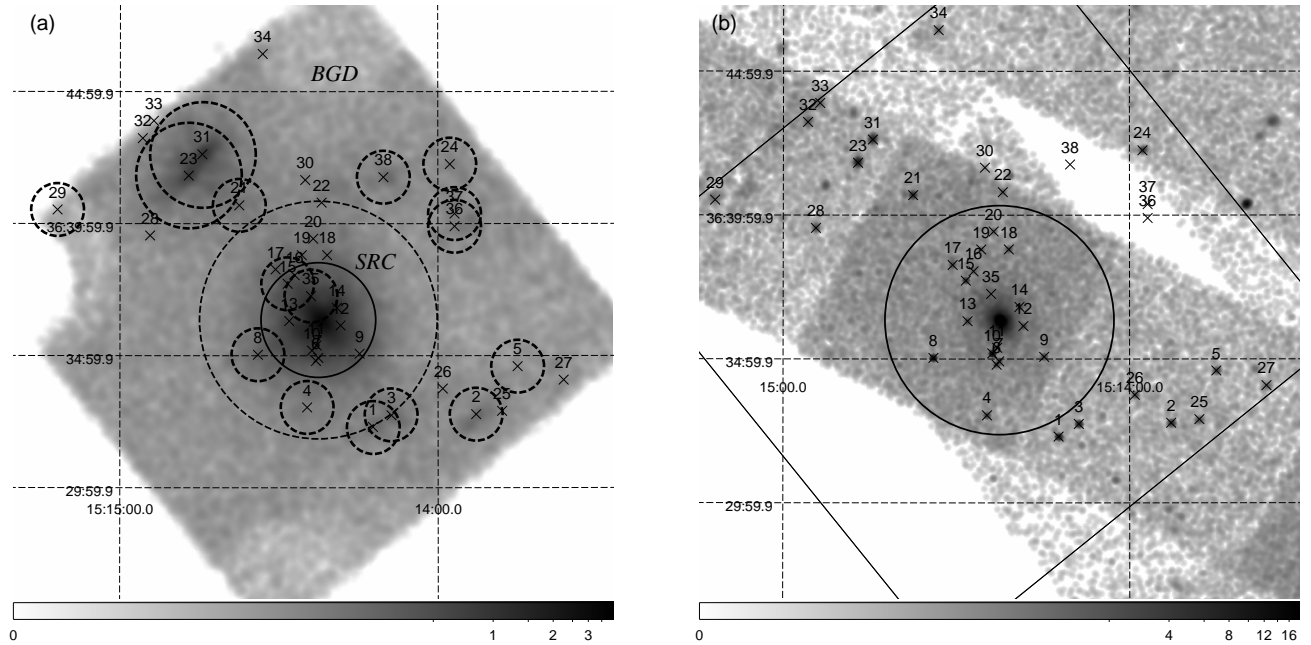


Fig. 1. (a) XIS image of MS 1512.4+3647 in the 0.5–7.0 keV energy range, smoothed with a Gaussian kernel of $\sigma = 16$ pixel $\simeq 17''$. The scale bar indicates the X-ray counts per pixel. The observed XIS0, 1, 3 images were added on the sky coordinates after removing calibration-source regions. The NXB was not subtracted, and the exposure and vignetting were not corrected. The removed regions of point sources from spectral analysis are indicated with dashed circles. The SRC and the BGD regions are within the solid circle and outside of the dashed circle, respectively. (b) ACIS image in 0.5–7.0 keV energy range, smoothed with a Gaussian kernel of $\sigma = 4$ pixel $\simeq 2''$. The Suzaku FOV and the virial radius are shown as the square and the solid circle on the image, respectively. The scale bar indicates the X-ray counts per pixel. The OBS1 and OBS2 images were added on the sky coordinates. The point sources detected with *wavdetect* or extracted from the CXC and 2XMMi catalogs are indicated with black crosses.

2.3. Response Files

Redistribution matrix files (RMFs) of the XIS were produced by *xisrmfgen*, and ARFs by *xissimarfgen* version 2010-11-05 (Ishisaki et al. 2007). The effect of contaminations on the optical blocking filter of the XIS is included in ARFs. Two types of ARFs were generated, A^U and A^I , for the uniform background emission and ICM emission, respectively. The input image of A^U is the uniform emission over a circular region of $20'$ radius, and the extract region of A^U is the BGD region of figure 1(a).

In order to make A^I , a background subtracted X-ray surface brightness profile of MS 1512.4+3647 was created from an ACIS 0.5–7.0 keV image of the Chandra OBS1 data. In this process, point sources were detected and removed from the ACIS image, using the *wavdetect* (Freeman et al. 2002) of CIAO with a detection threshold of 5σ . The background was extracted from a region outside the virial radius of MS 1512.4+3647 ($4'$). The center of the profile, $(\alpha, \delta) = (15^{\text{h}}14^{\text{m}}22^{\text{s}}6, +36^{\circ}36'21''.0)$, was determined from the position of X-ray emission centroid in the ACIS image. Then the profile was fitted with β -model (King 1962) of which parameters were determined through the least chi-square method. The resulting parameter set of β -model is $(r_c, \beta) = (21.7 \text{ kpc}, 0.53)$, where r_c is the core radius. The input image of A^I is the two dimensional β -model over the entire FOV of XIS, and the extract region of A^I is SRC region of figure 1(a).

RMFs and ARFs of the ACIS were produced by

specextract which is included in the CIAO package, together with source and background spectra of the ACIS.

3. Estimation of Background

Accurate estimation of background is the key to a spectral analysis of low surface brightness X-ray emission such as ICM. In the case of MS 1512.4+3647, the peripheral region of XIS (outside the virial radius, for example) where no ICM emission is expected can be used for that purpose. However, the background level of in the BGD region is not exactly the same as that in the SRC region. Therefore, we estimate non-X-ray background (NXB) and X-ray background (XRB) separately which are specific to the region to be analyzed. XRB is composed of cosmic X-ray background (CXB) and Galactic foreground emission (GFE). We identified point sources with Chandra and XMM-Newton data and excluded them.

3.1. Non-X-Ray Background

The NXB, which is the instrumental background except for the celestial X-ray background, was generated by *xisnxbgen*, which sorts night Earth data around an observation according to COR and makes a sum of the night Earth spectra weighted by the actual COR distribution of the observation (Tawa et al. 2008). Integrated period for the NXB is between ± 365 days of the Suzaku MS 1512.4+3647 observation. Night Earth events from the same detector area as the region to be analyzed in the

Table 1. Results of Model Fittings to XIS spectra of the BGD region

LHB			MWH			CXB		
kT (keV)	$Norm^*$	S^\dagger	kT (keV)	$Norm^*$	S^\dagger	Γ	S^\ddagger	χ^2/dof
$0.12^{+0.04}_{-0.02}$	$1.60^{+1.54}_{-0.68}$	$3.91^{+3.62}_{-1.74}$	$0.26^{+0.05}_{-0.03}$	$0.32^{+0.16}_{-0.20}$	$3.70^{+1.70}_{-2.47}$	1.41 (fix)	$5.09^{+0.12}_{-0.12}$	492.0/441

* Normalization of the *apec* component divided by 400π which is the area of the circular region ($r = 20'$ in radius) used for the uniform-sky ARF calculation. $Norm = 1/400\pi \int n_e n_H dV / [4\pi(1+z)^2 D_A^2] \times 10^{-20} \text{ cm}^{-5} \text{ arcmin}^{-2}$, where D_A is the angular diameter distance to the source.

† The 0.5–1.0 keV surface brightness in units of $10^{-9} \text{ erg s}^{-1} \text{ cm}^{-2} \text{ sr}^{-1}$.

‡ The 2.0–10.0 keV surface brightness in units of $10^{-8} \text{ erg s}^{-1} \text{ cm}^{-2} \text{ sr}^{-1}$.

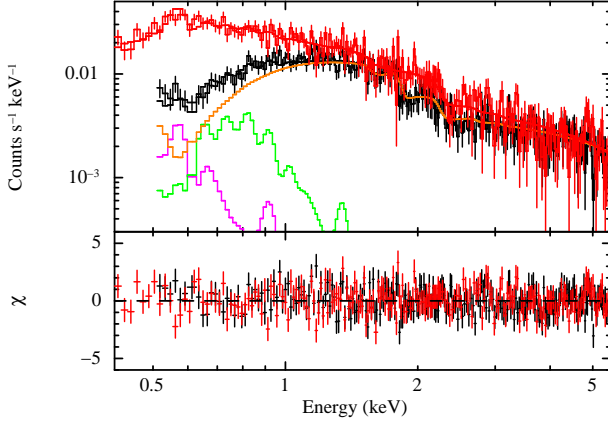


Fig. 2. NXB-subtracted XIS spectra of the BGD region, fitted with the X-ray background model described in section 3.5. Black and red are 0.5–5.5 keV XIS-FI (averaged over XIS0 and XIS3) and 0.4–5.5 keV XIS-BI spectra, respectively. The CXB component is shown in orange line, and the LHB and MWH emissions are indicated by magenta and green lines, respectively.

MS 1512.4+3647 XIS image were extracted in *xisnxbgen*. The systematic error associated with the NXB is $\pm 3\%$ (Tawa et al. 2008) in 1.0–12.0 keV energy range.

3.2. Point Sources

In the analysis of MS 1512.4+3647, the contribution of point sources has to be subtracted. The XIS image shown in figure 1(a) is thought to be contaminated by a number of point sources, but they are not resolved well due to a moderate spatial resolution of X-ray telescope (a half-power diameter of $\sim 2'$; Serlemitsos et al. 2007). To detect point sources, we utilized the Chandra Source Catalog (CSC; Evans et al. 2010) and the XMM-Newton 2nd Incremental Source Catalogue (2XMMi; Watson et al. 2009). The cataloged point sources are shown in figure 1 (serial numbers from 25 to 38). Position, photon index, and energy flux of these point sources are summarized in table 4. The detection limits of these catalogs are about $1 \times 10^{-14} \text{ erg s}^{-1} \text{ cm}^{-2}$ in 0.5–7.0 keV energy range for CSC and $1.5 \times 10^{-14} \text{ erg s}^{-1} \text{ cm}^{-2}$ in 2.0–12.0 keV energy range for 2XMMi. Because the cataloged sources are located far from MS 1512.4+3647, we also utilized the Chandra data to detect point sources around MS 1512.4+3647. The CIAO tool *wavdetect* (Freeman

et al. 2002) was executed on the 0.5–7.0 keV Chandra ACIS images of OBS1 with a detection threshold of 5σ . As shown in black crosses of figure 1(b) with serial numbers from 1 to 24, 24 point sources were detected in the ACIS FOV. The detection limit is about $2.0 \times 10^{-15} \text{ erg s}^{-1} \text{ cm}^{-2}$ in 2.0–10.0 keV energy range.

In the case of point sources detected with *wavdetect* in table 4, photon index, and energy flux were derived from spectral model fitting to the ACIS data, extracted from a circular region of $1''$ or $2''$ in radius depending on the source extent. Background was extracted from a source-free region of $1'$ in radius. In the fitting, the two sets of data (OBS1 and OBS2) were added, and absorbed power-law model, *wabs* \times *powerlaw*, was utilized with free or fixed (1.7) photon index depending on statistics. Column density was fixed to the Galactic value of $1.4 \times 10^{20} \text{ cm}^{-2}$. The results are shown in figure 9. The energy flux of the point sources ranges from $\sim 10^{-15}$ to $\sim 10^{-13} \text{ erg s}^{-1} \text{ cm}^{-2}$. Some sources which were detected by *wavdetect* are also listed in CSC. We confirmed that energy flux obtained by *wavdetect* and CSC is consistent within errors. In following spectral analysis, point sources with energy flux larger than $1.6 \times 10^{-14} \text{ erg s}^{-1} \text{ cm}^{-2}$ in 2.0–10.0 keV are excluded in circular regions of $1'$ or $2'$ radius depending on source extent, as shown in figure 1(a). The point sources with energy flux lower than $1.6 \times 10^{-14} \text{ erg s}^{-1} \text{ cm}^{-2}$ in 2.0–10.0 keV are included in the CXB model (detailed in section 3.3), corresponding to 30% of CXB intensity, and have roughly consistent numbers with the $\log N$ – $\log S$ relation (Kushino et al. 2002).

3.3. Cosmic X-Ray Background

After the removal of point sources, there remains contribution from unresolved extragalactic sources (CXB) to XRB. In the spectral analysis, an absorbed power-law model with a fixed photon index of 1.41 (Kushino et al. 2002) *wabs* \times *powerlaw* was used as the CXB model. Intensity of the CXB after the removal of point sources with flux higher than $1.6 \times 10^{-14} \text{ erg s}^{-1} \text{ cm}^{-2}$ in 2.0–10.0 keV is calculated to be $(3.80^{+0.46}_{-1.52} \pm 0.38) \times 10^{-8} \text{ erg s}^{-1} \text{ cm}^{-2} \text{ sr}^{-1}$ (90% statistical and systematic errors) from equation (6) of Kushino et al. (2002).

3.4. Galactic Foreground Emission

GFE typically consists of an unabsorbed plasma (LHB; representing the local hot bubble and the solar-wind

charge exchange) and an absorbed plasma (MWH; representing the Milky Way halo). To express the GFE, we employed two-temperature model, $apec_1 + wabs \times apec_2$, according to Tawa et al. (2008), where the *apec* model is a thin thermal plasma emission model detailed in Smith et al. (2001). The redshift and abundance of the two *apec* components were fixed to zero and unity, respectively.

3.5. Spectral Analysis of Background Region

In order to estimate the XRB around MS 1512.4+3647, we extracted FI and BI spectra from a background region of the XIS image (BGD region in figure 1(a)). This BGD region is further than $1.1r_{200}$ of MS 1512.4+3647, and the contribution of ICM is 8% of XRB there, assuming the ICM extends beyond r_{200} following the β -model profile obtained in section 2.3 with the point spread function of XRT. We fitted NXB-subtracted FI and BI spectra of the BGD region simultaneously with a model of $apec_1 + wabs \times (apec_2 + powerlaw)$ that represents the CXB and GFE emissions in 0.5–5.5 keV for FI and 0.4–5.5 keV for BI. Galactic absorption was fixed to the Galactic value of $1.4 \times 10^{20} \text{ cm}^{-2}$. The ARFs of A^U were used for the model fitting. The best-fit parameters for the BGD region are summarized in table 1, and the spectra are shown in figure 2. The fit is moderately good with the probability that chi squared value becomes larger than the fitting value is 0.047.

The 2.0–10.0 keV surface brightness of the CXB component is $(5.09 \pm 0.12 \pm 0.27) \times 10^{-8} \text{ erg s}^{-1} \text{ cm}^{-2} \text{ sr}^{-1}$ (90% statistical and systematic errors), where the systematic error of 5.4% is derived by scaling the fluctuation analysis with Ginga (Hayashida 1989) to our flux limit and FOV of $1.6 \times 10^{-14} \text{ erg s}^{-1} \text{ cm}^{-2}$ and 0.06 deg^2 , respectively (detailed in Hoshino et al. 2010; Akamatsu et al. 2011). This CXB fluctuation is consistent with Nakazawa et al. (2009) scaled by HEAO-1, -2 results. The obtained surface brightness is slightly larger ($\sim 25\%$) than the calculated value described in section 3.3, although consistent within statistical and systematic errors. In the spectral analysis of the ICM, we also tried the calculated CXB surface brightness instead of that obtained from the BGD region, and confirmed that the fitting results did not change significantly.

The temperature and surface brightness of LHB are $kT = 0.12_{-0.02}^{+0.04} \text{ keV}$ and $(3.91_{-1.74}^{+3.62}) \times 10^{-9} \text{ erg s}^{-1} \text{ cm}^{-2} \text{ sr}^{-1}$ in 0.5–1.0 keV energy range, respectively. Those of MWH are $kT = 0.26_{-0.03}^{+0.05} \text{ keV}$ and $(3.70_{-2.47}^{+1.70}) \times 10^{-9} \text{ erg s}^{-1} \text{ cm}^{-2} \text{ sr}^{-1}$ in 0.5–1.0 keV energy range, respectively. The obtained temperatures of LHB and MWH are consistent with typical values of these GFE components (Lumb et al. 2002; Yoshino et al. 2009).

4. Spectral Analysis and Results

For the spectral analysis of the ICM in MS 1512.4+3647, we extracted XIS spectra within a circular region of $2.2'$ in radius ($\sim 0.6r_{200}$, shown as the SRC region in figure 1(a)), centered on $(\alpha, \delta) = (15^{\text{h}}14^{\text{m}}22^{\text{s}}.6, +36^{\circ}36'21''.0)$. The center was determined

from the position of X-ray emission centroid in the Chandra ACIS image, as described in section 2.3. The radius of extraction was determined to maximize significance of the ICM signal with respect to the noise, composed of the NXB, CXB, and GFE. The three point sources within the SRC region were masked by a circle of $1'$ radius (dashed circles in figure 1(a)). Since MS 1512.4+3647 is rather distant, X-ray signals from core regions and outer regions are highly mixed due to the Suzaku PSF. Therefore, we did not study radial dependence of parameters such as temperature, gas density, and metal abundances. After extracting spectra of the XIS0, XIS1, and XIS3, we created a single XIS-FI spectra by averaging the XIS0 and XIS3 spectra.

In figure 3(a), we compared raw SRC spectra (black cross for XIS-FI and gray cross for XIS-BI) with corresponding NXB spectra (circled black cross and circled gray cross). The raw SRC spectra have significant excess in 0.4–6.5 keV (XIS-FI) and 0.3–6.5 keV (XIS-BI), respectively, due to the ICM and XRB emission. In the higher energies than 6.5 keV, the raw SRC spectra overlap with the NXB spectra, because the NXB is dominant in the energy range. Figure 3(b) is NXB-subtracted SRC spectra (black cross for XIS-FI and gray cross for XIS-BI) with the best-fit XRB model for the BGD region described in section 3.5 (black and gray solid line). The signal from ICM is significantly detected in 0.5–6.5 keV (XIS-FI) and 0.4–6.5 keV (XIS-BI), respectively. The emission lines from ionized metals, especially the redshifted Fe-K line, are seen in the spectra of figure 3(b). These lines are clearer as excess in each atomic-line energy of Ne, Mg, Si, S, Fe, and Ni shown in figure 4, where we fitted the NXB-subtracted SRC spectra with $wabs \times brems + XRB$ model.

In order to determine metal abundances, the NXB-subtracted XIS-FI and XIS-BI SRC spectra were fitted with an absorbed single-temperature thin-thermal emission model (1T), $wabs \times vapec$ (*vapec*: Smith et al. 2001) added to the XRB model (section 3.5), in 0.5–6.5 keV energy range as shown in figure 5. In this fitting, the BGD spectra (figure 2) were simultaneously fitted with the same XRB model to determine the XRB in MS 1512.4+3647. For the SRC spectra, we utilized the NXB and response (RMF and ARF) files of the SRC region (section 2.3), while those of the BGD region were used for the BGD spectra. The uniform sky ARF, A^U , and the β -model ARF, A^I , were assigned to the XRB model and the ICM model, respectively. In the 12 metal abundances in *vapec*, we set He = C = N = O = one solar abundance because the emission lines from these elements are out of energy range. The emission lines from Al, Ar, and Ca are not significantly detected (figure 4). Then we set S = Ar = Ca, and set Al as free parameter. We also examined two cases: 1) free parameters of S, Ar, and Ca, 2) linked parameters of Mg = Al. The errors of S and Mg abundances increased about 5% in the case 1) and 10% in the case 2), respectively. The other abundances, Ne, Si, Fe, and Ni, were free. Therefore, we had seven free metal-abundance parameters. The hydrogen column density was fixed to the Galactic value of $1.4 \times 10^{20} \text{ cm}^{-2}$ and redshift was

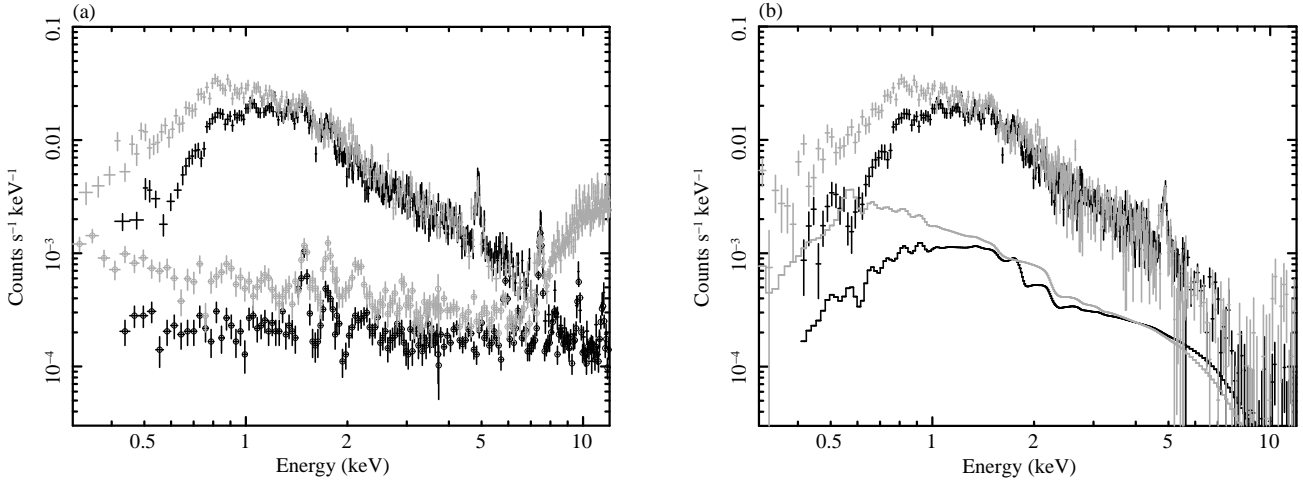


Fig. 3. (a) Raw XIS spectra of the SRC region and NXB spectra extracted from the same region. Black and gray crosses are 0.3–12.0 keV XIS-FI (averaged over XIS0 and XIS3) and XIS-BI raw spectra, respectively, and circled black and gray crosses are XIS-FI and XIS-BI NXB spectra, respectively. (b) NXB-subtracted spectra of the SRC region with the best-fit X-ray background model described in section 3.5.

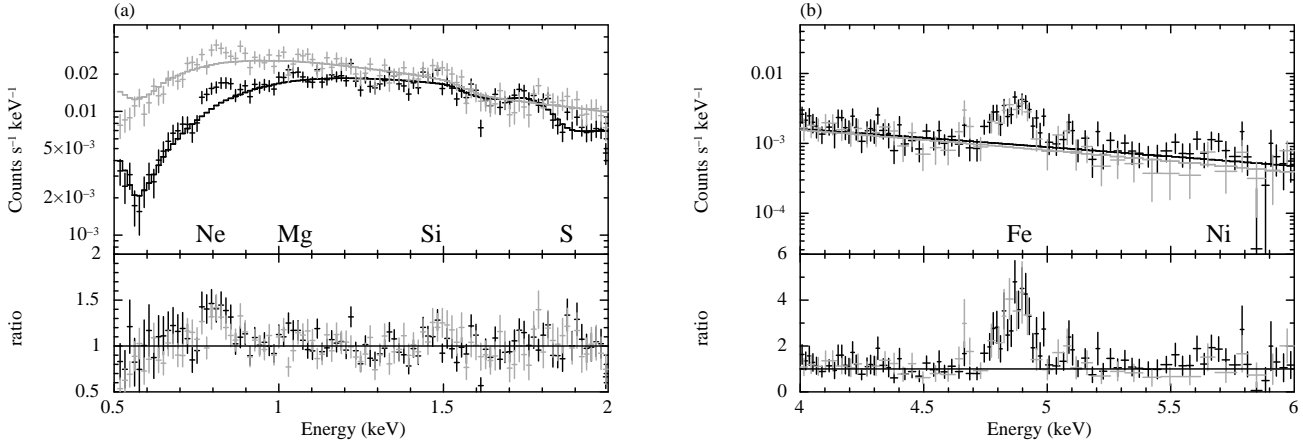


Fig. 4. (a) XIS-FI (black) and XIS-BI (gray) spectra around the Ne, Mg, S, and Si emission lines extracted from the SRC region, with the best-fit $wabs \times brems$ model (solid lines). The positions of the redshifted metal lines are also indicated. The lower panel shows the ratio of the data to model. (b) The same as panel(a), but for spectra around the Fe and Ni emission lines.

also fixed to 0.372. In the XRB model, all parameters were free except for the photon index of the CXB model (section 3.5). The fitting result is summarized in table 2. The Al abundance is not determined significantly and we don't indicate about Al abundance in the following analysis.

The metal abundances of individual elements are determined in 3σ significance except for Ne and Mg which have large error bars. These metal abundances of MS 1512.4+3647 are similar to those of nearby clusters (e.g. Sato et al. 2009b). The best-fit luminosity and temperature are $(2.9 \pm 0.2) \times 10^{44}$ erg s^{-1} in 2.0–10.0 keV energy range and 3.28 ± 0.09 keV, respectively. The temperature is consistent with ASCA results (Ota 2000) within statistical errors. The luminosity is also consistent with the ASCA value (Ota 2000) when it is corrected for the difference of integrated areas between ASCA GIS and Suzaku XIS.

The ICM in MS 1512.4+3647 is considered to have

temperature structures, especially between the core and outer regions. If this is true, a multi-temperature model may reproduce the SRC spectra better. We tried two-temperature model (2T), $wabs \times (vapec + vapec)$. In the 2T model, each metal abundance was tied between the two thermal components and Ne abundance was fixed to one solar value. Therefore, in the 2T model, only one temperature parameter was added as a new free parameter to the 1T model. The fitting result is summarized in table 2. From the F-test, we cannot decline the null hypothesis at 5% significance level that adding one thermal component from 1T to 2T does not improve the fit, because the P-value is 0.137. In fact, the two ICM temperatures are obtained only as lower limits, and the metal abundances are consistent with those of the 1T model within statistical errors. Thus, the 1T model is statistically sufficient to reproduce the data. It suggests that the potential temperature drop in the very central region is moderate, if any.

Table 2. Results of Model Fittings to the XIS spectra of SRC region.

Model	kT1 (keV)	kT2 (keV)	Ne (solar)	Mg (solar)	Si (solar)	S=Ar=Ca (solar)	Fe (solar)	Ni (solar)	$\chi^2/\text{d.o.f.}$
1T	$3.28^{+0.09}_{-0.09}$	—	< 2.26	$0.64^{+0.54}_{-0.51}$	$0.63^{+0.21}_{-0.20}$	$0.42^{+0.23}_{-0.23}$	$0.64^{+0.08}_{-0.07}$	$1.94^{+1.06}_{-1.02}$	1087.8/1014
2T	$0.79 <$	$0.92 <$	1 (fix)	$0.73^{+0.48}_{-0.26}$	$0.67^{+0.17}_{-0.11}$	$0.49^{+0.20}_{-0.12}$	$0.62^{+0.06}_{-0.07}$	$2.00^{+0.91}_{-0.90}$	1085.4/1013
CXB−6%	$3.30^{+0.08}_{-0.09}$	—	< 2.49	$0.65^{+0.55}_{-0.51}$	$0.64^{+0.21}_{-0.20}$	$0.42^{+0.23}_{-0.23}$	$0.65^{+0.08}_{-0.08}$	$2.02^{+1.07}_{-1.03}$	1095.0/1015
CXB+6%	$3.29^{+0.09}_{-0.04}$	—	< 2.26	$0.65^{+0.54}_{-0.52}$	$0.64^{+0.21}_{-0.23}$	$0.42^{+0.21}_{-0.21}$	$0.64^{+0.04}_{-0.07}$	$1.94^{+1.04}_{-0.76}$	1083.3/1015
NXB±3%	$3.28^{+0.08}_{-0.09}$	—	< 2.27	$0.64^{+0.54}_{-0.51}$	$0.63^{+0.21}_{-0.20}$	$0.42^{+0.23}_{-0.23}$	$0.64^{+0.08}_{-0.07}$	$1.94^{+1.06}_{-1.02}$	1080.8/1014
CONTAMI−10%	$3.38^{+0.11}_{-0.09}$	—	< 2.01	$0.81^{+0.58}_{-0.54}$	$0.74^{+0.23}_{-0.21}$	$0.51^{+0.25}_{-0.22}$	$0.64^{+0.08}_{-0.08}$	$1.99^{+1.09}_{-1.06}$	1092.3/1014
CONTAMI+10%	$3.19^{+0.04}_{-0.09}$	—	< 2.59	$0.51^{+0.52}_{-0.48}$	$0.55^{+0.20}_{-0.19}$	$0.35^{+0.22}_{-0.21}$	$0.64^{+0.08}_{-0.07}$	$1.93^{+1.04}_{-1.00}$	1092.8/1014

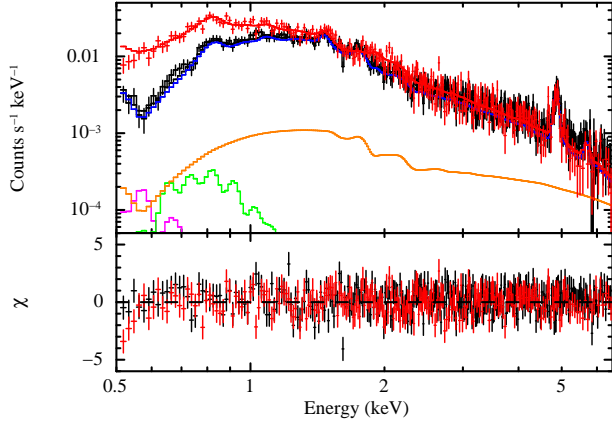


Fig. 5. NXB-subtracted spectra of the SRC region. Black and red are 0.5–6.5 keV XIS-FI (averaged over XIS0 and XIS3) and XIS-BI spectra, respectively. These spectra are fitted simultaneously with the 1T model added to the XRB model (section 3.5). Black and red lines are the best-fit model of the XIS-FI and XIS-BI, respectively. For the XIS-FI, model components of the ICM (1T), LHB, MWH, and CXB are shown in blue, magenta, green, and orange, respectively. The lower panel shows the fit residuals in units of σ . XRB spectra are not plotted here for clarity.

Finally, we tested the robustness of our results against the systematic errors associated with the background estimation and the contamination estimation on the blocking filter. We repeated the spectral fit by changing the NXB intensity by $\pm 3\%$. The error due to the CXB intensity fluctuation was also examined by varying the CXB normalization by 6%, which was derived by scaling the Ginga results with the XIS sensitivity and the field of view (section 3.5). The systematic error in the contamination thickness of the XIS blocking filter is typically 10%, and we evaluated its effect through spectral fits by adjusting the detector response which included the contamination thickness. The results are summarized in table 2. The temperature and abundances did not change significantly by these systematic uncertainties. We employed the systematic errors, σ_{NXB} , σ_{CXB} , and σ_{CONTAMI} , by examining the change of the fitted parameters in table 2. As a result, σ_{CXB} and σ_{NXB} are always less than 10% of the statistical errors, and σ_{CONTAMI} is comparable to the statistical error for the temperature and roughly 50% of that for the abundances of Mg, Si and S. In the following analysis we used the error defined by

$$\sigma_{\text{error}} = (\sigma_{\text{NXB}}^2 + \sigma_{\text{CXB}}^2 + \sigma_{\text{CONTAMI}}^2)^{1/2}.$$

From the spectral analysis of Suzaku data, we obtained metal abundances of MS 1512.4+3647, which are similar to those of nearby clusters. To study the contributions of two types of supernovae (SNe Ia and SNe II), we derived the relative abundance ratios to Fe by calculating confidence contours between the Fe abundance and another abundance. The results are shown in figure 6 and table 3. The relative abundance ratio (90% confidence level) is determined from the slope of two lines which pass the origin (zero abundance point) and come in contact with the 90% confidence region. The abundance ratios are ~ 1 solar ratio within statistical errors (table 3).

Figure 7(a) shows metal to Fe number ratios in MS 1512.4+3647, obtained from the present Suzaku observation. In comparison, the same ratios for nearby clusters observed with Suzaku are also plotted. The values are for the radius range of 0.05–0.1 r_{180} , and the clusters are AWM 7 ($z = 0.0172$; Sato et al. 2008), Abell 262 ($z = 0.0163$; Sato et al. 2009b), Centaurus cluster ($z = 0.0104$; Sakuma et al. 2011), NGC 5044 ($z = 0.0090$; Komiyama et al. 2009), NGC 1550 ($z = 0.0124$; Sato et al. 2010), HCG 62 ($z = 0.0145$; Tokoi et al. 2008), and NGC 507 ($z = 0.0165$; Sato et al. 2009a). The figure also shows the XMM-Newton result by de Plaa et al. (2007), indicating the average values for 22 clusters ($0.0214 \leq z \leq 0.1840$).

Figure 7(a) shows that MS 1512.4+3647 has the metal to Fe number ratios consistent with those in nearby clusters within the statistical and systematic errors, noting that Ne and Mg lines had insufficient statistics and only upper limits were obtained. In the same figure, the expected abundance patterns of SNe Ia and II yields, based on the calculation by Iwamoto et al. (1999) and Nomoto et al. (2006), are also plotted. We assumed the W7 model for SNe Ia, along with the Salpeter initial mass function (IMF) for stellar masses from 10 to 50 M_{\odot} with a progenitor metallicity of $Z = 0.02$ for SNe II. The observed number ratios for Ne, Mg, Si, S, and Ni over Fe all lie between the SN Ia and SN II values. Therefore, both types of the supernova are considered to have enriched the ICM of the clusters shown in figure 7(a), including MS 1512.4+3647.

If we assume the metals synthesized in clusters have been kept within the cluster system, the ratio of cumulative number of SN II explosions to that of SN Ia explosions in each cluster can be estimated from the abundance pattern of metals contained in clusters, because the

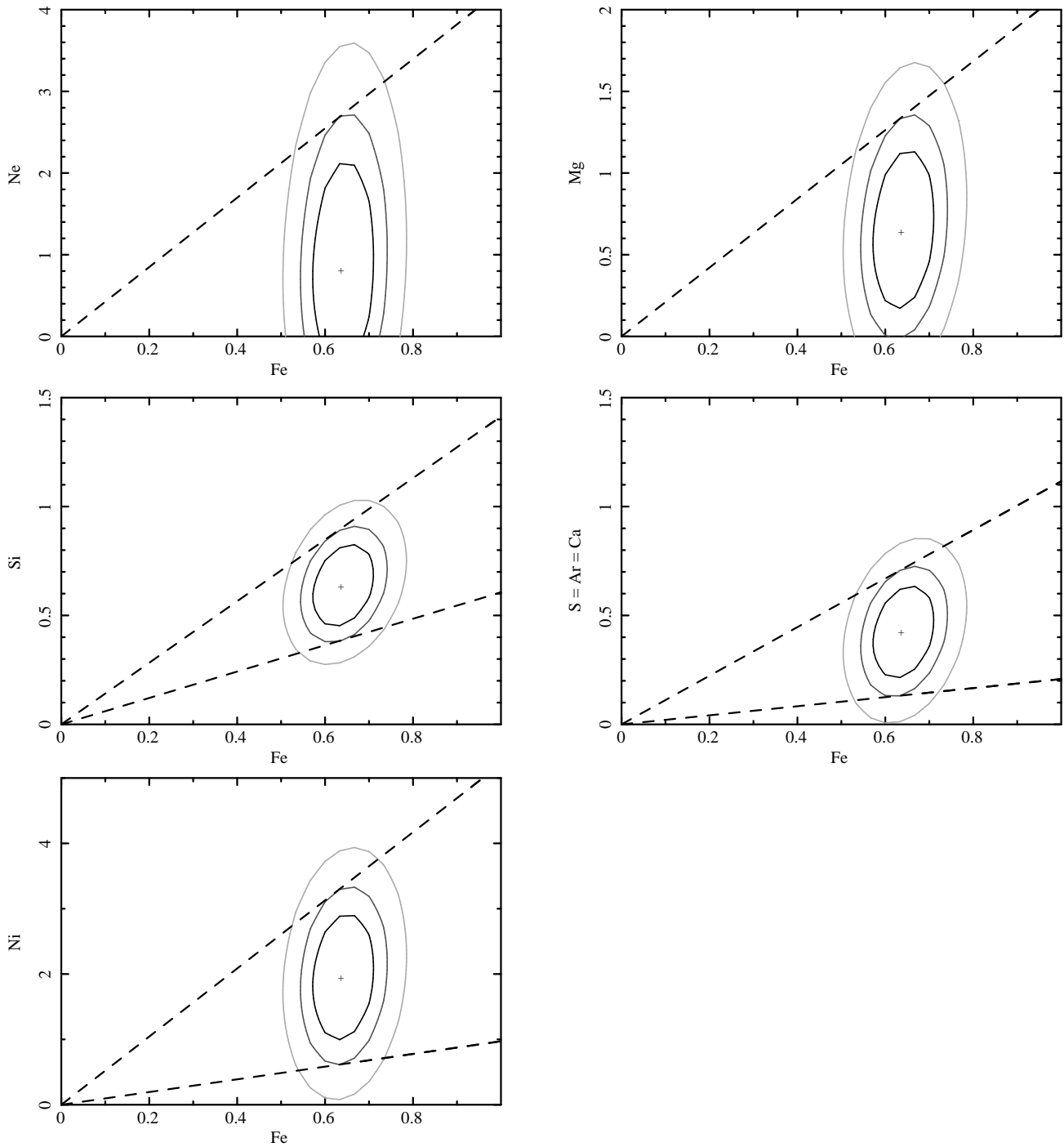


Fig. 6. Confidence contours between a metal (Ne, Mg, Si, S, or Ni) and Fe abundances. The black, gray, and light gray contours represent 68%, 90%, and 99% confidence regions, respectively.

two types of supernova give significantly different metal yields. Most of Ne and Mg are synthesized by SN II, while Fe and Ni are mostly produced by SN Ia. The abundance pattern was fitted by the sum of the expected abundance patterns of SN Ia and SN II (black solid line in figure 7(b)). Free parameters in the fit are two normalizations of the abundance patterns of the SN Ia and SN II metal yields. In the actual fit, however, free parameters were chosen to be the normalizations of SNe Ia (N_1) and the number ratio of SNe II to SNe Ia (N_2/N_1), because N_1 could be constrained well with the relatively small error in the Fe abundance. The derived parameters are $N_2/N_1 = 3.6 \pm 2.9$. Sato et al. (2007b) reported the supernova ratio, N_2/N_1 , for nearby four clusters to be ~ 3.5 . de Plaa et al. (2007) also showed that the number ratio of core-collapsed SNe (SNe II+Ib+Ic) to SNe Ia is ~ 3.5 , based on XMM-Newton observations. In figure 8(a), the N_2/N_1 ratio of MS 1512.4+3647 is compared with those of nearby clusters and groups, which are NGC 5044, Abell 262, and four other clusters studied by Sato et al. (2007b). The value of MS 1512.4+3647 has a rather large error and is clearly consistent with those of nearby clusters.

5. Discussion

5.1. Contributions from SNe Ia and SNe II

Figure 8(a) also shows a curve based on a simple model. For the model, we adopted the star formation history in equation (5) of Strolger et al. (2004), which is based on field galaxy data, as the time evolution of the SN II frequency, and the gaussian model for the SN Ia time evolution (see figure 14 of Strolger et al. 2004). The present result gives little constraint to the model of the supernova history, but the improvement of sensitivity planned in future missions will give a meaningful result.

In figure 8(b), the numbers of SNe Ia and SNe II explosions estimated within $0.3r_{200}$ are plotted against the gas mass. The SN numbers of MS 1512.4+3647 are compared with those of four nearby clusters by Sato et al. (2007b), which are AWM 7, A1060, NGC 507, and HCG 62. The radius of $0.3r_{200}$ is adopted by following reasons: (1) the systematic and statistical errors of abundance profiles become large toward larger radii, (2) the effect of cool core becomes relatively larger for smaller radii, and (3) $\sim 90\%$ of the detected photons within $0.6r_{200}$ actually originated from within $0.3r_{200}$, simulated with the spectrum of MS 1512.4+3647. We evaluated systematic error due to the scaling at several radii and concluded that it is minimized at $\sim 0.3r_{200}$.

The integrated mass of the ICM in MS 1512.4+3647 within $0.3r_{200}$ is estimated as follows. Because the normalization of the *vaptec* model was scaled to the value of the input XIS image size for the A^I in the spectral analysis, we derived the true normalization within $0.3r_{200}$ to multiply a factor, (counts within $0.3r_{200}$)/(counts of whole region), to the normalization of the *vaptec* model. The energy flux within $0.3r_{200}$ using this method is consistent with the one of the

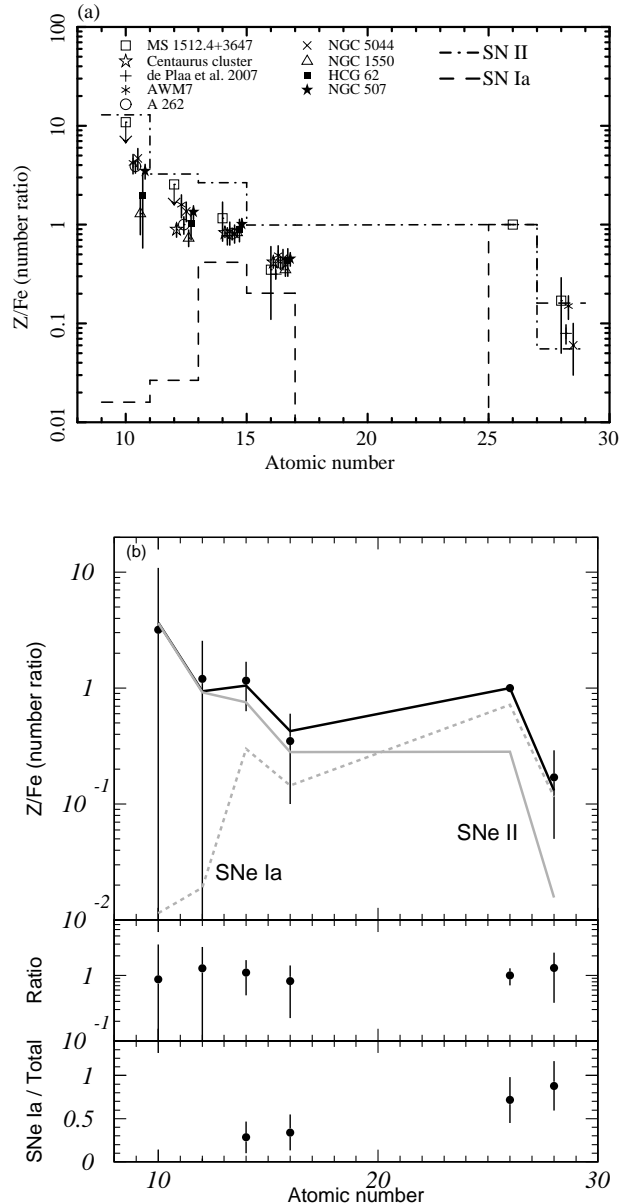


Fig. 7. (a) The abundance ratios of Ne, Mg, Si, S, and Ni to Fe within $0.6r_{200}$. Those of nearby clusters are also plotted. The supernova yield models for SN Ia (W7: Iwamoto et al. 1999) and SN II ($Z = 0.02$ and Salpeter IMF: Nomoto et al. 2006) are plotted in black dashed and dot-dashed lines, respectively. (b) Top panel shows the abundance ratios within $0.6r_{200}$ (black points) fitted by $N_1 + (N_2/N_1)$ (black line). Gray dashed and solid lines correspond to the contributions of SNe Ia and SNe II, respectively. Middle and bottom panels indicate ratios of data to the best fit model, and fractions of the SNe Ia contribution to total metal numbers of individual elements, respectively.

Table 3. The metal abundance ratio to Fe.

Model	Ne/Fe (solar)	Mg/Fe (solar)	Si/Fe (solar)	S/Fe (solar)	Ni/Fe (solar)
1T	< 4.28	< 2.09	$0.99^{+0.42}_{-0.38}$	$0.66^{+0.45}_{-0.45}$	$3.03^{+2.16}_{-2.06}$
2T	—	$1.18^{+1.10}_{-1.03}$	$1.09^{+0.45}_{-0.40}$	$0.79^{+0.54}_{-0.51}$	$3.25^{+2.48}_{-2.20}$
CXB−6%	< 4.55	< 2.08	$0.98^{+0.42}_{-0.39}$	$0.65^{+0.46}_{-0.45}$	$3.11^{+2.23}_{-2.05}$
CXB+6%	< 4.27	< 2.11	$1.00^{+0.42}_{-0.39}$	$0.66^{+0.46}_{-0.45}$	$3.04^{+2.26}_{-2.05}$
NXB±3%	< 4.23	< 2.09	$0.99^{+0.42}_{-0.38}$	$0.66^{+0.45}_{-0.45}$	$3.03^{+2.24}_{-2.06}$
CONTAMI−10%	< 3.86	$1.27^{+1.21}_{-1.08}$	$1.16^{+0.39}_{-0.41}$	$0.80^{+0.49}_{-0.48}$	$3.11^{+2.29}_{-2.12}$
CONTAMI+10%	< 4.74	< 1.82	$0.85^{+0.39}_{-0.36}$	$0.54^{+0.42}_{-0.42}$	$2.99^{+2.15}_{-1.99}$

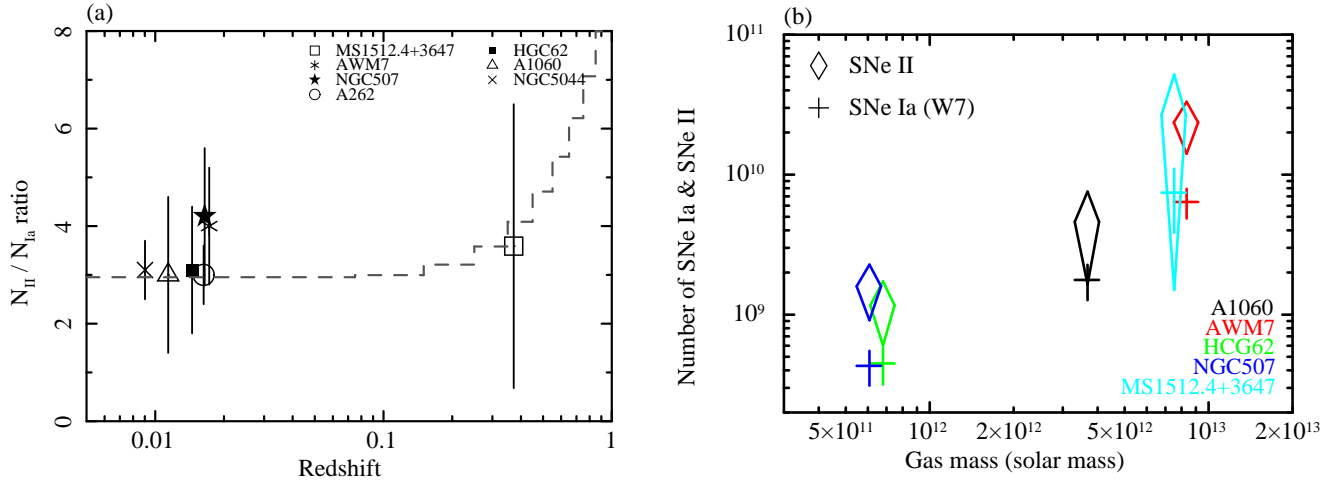


Fig. 8. (a) Number ratios of SNe II to SNe Ia plotted against redshift. Dashed gray line indicates expected model, where SNe II and SNe Ia model are taken from equation (5) and figure 14 of Strolger et al. (2004), respectively. (b) Integrated numbers of SN Ia (cross) and SNe II (diamond) plotted against the gas mass within $0.3r_{200}$. Systematic errors described in section 5.1 are included in this figure. In both (a) and (b), the results of nearby clusters are also plotted.

Chandra results. By comparing the obtained normalization to the volume integration of squared density profile (3-dimensional β -model; $\rho_{\text{gas}}(r) = \rho_0(1 + (r/r_{\text{core}}))^{-3\beta/2}$), we derived the normalization of 3-dimensional β -model as $\rho_0 = 6.4 \times 10^{-2}$. Where ρ and r are gas density and radius from cluster center, respectively. Finally, the integrated mass of the ICM within $0.3r_{200}$ is estimated as $7.53 \times 10^{12} M_{\odot}$ by integrating the 3-dimensional β -model. The cumulative numbers of SN Ia and SN II explosions can be estimated from the mass of metals contained in clusters. Based on the metal abundances and the estimated mass of the ICM, we calculated the mass of individual metals. From the metal mass and relative numbers of SN Ia and SN II shown in figure 7(b), the cumulative numbers of SN Ia and SN II within $0.3r_{200}$ are derived as $N_{\text{SN Ia}} = (7.4 \pm 2.9) \times 10^9$ and $N_{\text{SN II}} = (2.7 \pm 2.4) \times 10^{10}$.

For nearby four clusters, the SN numbers and gas mass are scaled to the values within $0.3r_{200}$. The gas density profiles and metal abundances of these nearby clusters are spatially resolved up to $0.36r_{200}$, $0.26r_{200}$, $0.25r_{200}$, $0.22r_{200}$ for AWM 7, A1060, NGC 507, and HCG 62, respectively. Each gas mass is scaled using 3-dimensional β -model. The β values and core radii were taken from the literature (Sato et al. 2008; Sato et al. 2007a;

Sato et al. 2009a; Tokoi et al. 2008), and normalizations were derived by fitting gas mass profiles shown in the literature (Sato et al. 2008; Sato et al. 2007a; Sato et al. 2009a; Tokoi et al. 2008). We assumed that the numbers of SN Ia and SN II are proportional to the metal mass of Fe and Mg, respectively. Namely, $N_{\text{SN Ia}} \propto M_{\text{Fe}}$ and $N_{\text{SN II}} \propto M_{\text{Mg}}$. Using above assumption, the metal mass of Fe and Mg are derived from the metal mass profile $\rho_{\text{metal}}(r) = Z_{\text{metal}}(r) \times \rho_{\text{gas}}(r)$ integrated up to $0.3r_{200}$, where we adopted a β -model for the metal abundance profile, $Z_{\text{metal}}(r) = Z_0(1 + (r/r_{\text{core}}))^{-\alpha}$ (De Grandi et al. 2004). Lastly, we multiplied scaling factor, $f = M_{\text{metal}}(0.3r_{200})/M_{\text{metal}}(r_{\text{obs}})$, to the numbers of SN Ia and SN II within the individual observed radii.

There are several systematic errors due to the scaling method. We roughly estimated the systematic errors for the cumulative numbers estimations of MS 1512.4+3647, and the gas mass scaling of nearby clusters as 30%, and 20%, respectively (detailed in appendix 2). These systematic errors are taken into account in figure 8(b). Figure 8(b) shows that both the SN Ia and SN II numbers are in good positive correlation with the gas mass, including MS 1512.4+3647 which is at a medium redshift, though the SN Ia number of MS 1512.4+3647 is

slightly above the correlation.

5.2. Implications for Metal Enrichment History

The supernova numbers in MS 1512.4+3647 lie on the correlation between the gas mass and the numbers of SN Ia and SN II as shown in figure 8(b). Figure 8 indicates that the integrated number of SNe ($N_{\text{SN Ia}}$ and $N_{\text{SN II}}$) range 4×10^8 – 8×10^9 and 1×10^9 – 2×10^{10} , respectively, in the range of two figures of gas mass. This suggests that this cluster has already experienced as many supernovae as nearby clusters. The past history of SN II explosions is correlated with the star formation history (SFH), IMF, and the lifetime function (e.g. Borgani et al. 2002). Since massive stars above $\sim 8 M_{\odot}$ cause a core collapse with a short lifetime, the history of SN II should follow the curve of SFH, which is relatively flat at $z > 2$, peaked at $1 < z < 2$, and then decreases by about one order of magnitude toward $z \sim 0$ (e.g. Strolger et al. 2004). This scenario is consistent with the SN II contribution in MS 1512.4+3647 (figure 8(b)) which is similar to that in AWM 7. For example, in the SFH models (M1 and M2) in Strolger et al. (2004), the number of star formation per unit volume at $0 < z < 0.4$ is only $\sim 10\%$ of the integrated value in $0 < z < 6$. This suggests that the number of SN II in MS 1512.4+3647 would be lower than the nearby values by about $\sim 10\%$, which is within the error as seen in figure 8(b).

The history of the SN Ia rate is more complicated, because the lifetime function of binary systems needs to be convolved with the star formation rate (e.g. Borgani et al. 2008). In general, the SN Ia rate is peaked later in time (at smaller z) and prolonged longer than the SN II rate history. In fact, a mild decrease of the SN Ia rate in the cluster environment is found from $z \sim 1$ to $z \sim 0$ by a factor of $2 \sim 10$ (Gal-Yam et al. 2002). Our result in figure 8(b) suggests a low SN Ia rate in $0 < z < 0.37$, since the SN Ia numbers normalized by the gas mass are the same between MS 1512.2+3647 and nearby clusters. If one assumes the evolution of the SN Ia rate implied from the field galaxy data (for example, model 1N2.3 in solid line in figure 10b of Loewenstein 2006), the number of SN Ia would increase by $\sim 40\%$ from $z = 0.37$ to $z = 0$, namely in about 4 Gy. In this case, the SN Ia point of MS 1512.4+3647 in figure 8(b) would exceed the level of AWM 7 when 4 Gy passed, causing some deviation (from 0.7σ to 1.8σ) from the present linear relationship in this figure. Therefore, models of the SN Ia evolution with steeper gradient and/or more contribution at larger redshifts (for example, model 2H1.05WxSt1 in solid line in figure 11b of Loewenstein 2006) would be favored. Same results are reported from several observations of SNe Ia (Mannucci, Della Valle & Panagia 2006; Maoz, Mannucci & Brandt 2012).

6. Conclusion

Based on the Suzaku observation of MS 1512.4+3647, we derived metal abundances of Ne, Mg, Si, S, Fe and Ni in the ICM. All the elements show the similar abun-

dance values around ~ 0.5 solar, and the abundance ratios relative to the Fe value are approximately 1 solar except for Ni. The number ratios of Ne, Mg, Si, S, and Ni to Fe in MS 1512.4+3647 are consistent with those for nearby clusters within the errors and lie between the expected values of SN II and SN Ia yields. Both SN Ia and SN II products are considered to have enriched the ICM of MS 1512.4+3647 to the same amount as in nearby clusters.

The integrated number of SNe Ia ($N_{\text{SN Ia}}$) and the number ratio of SNe II to SNe Ia ($N_{\text{SN II}}/N_{\text{SN Ia}}$) were derived to be $N_{\text{SN Ia}} = (7.4 \pm 2.9) \times 10^9$ and $N_{\text{SN II}}/N_{\text{SN Ia}} = 3.6 \pm 2.9$, respectively. The number ratio of SNe II to SNe Ia in MS 1512.4+3647 is consistent with those in nearby clusters within the errors. The integrated numbers of both SNe Ia and SNe II explosions are comparable to those in nearby clusters of galaxies when normalized by the gas mass. This similarity indicates that MS 1512.4+3647 has already experienced as many SNe Ia and SNe II supernovae as in nearby clusters.

Massive stars heavier than $\sim 8 M_{\odot}$ cause a core collapse in a short lifetime, and the past SN II rate is expected to approximately follow the SFH. The observed feature of SNe II in MS 1512.4+3647 is consistent with this standard scenario of the SN II history. The similarity in the number of SNe Ia to nearby clusters suggests an SN Ia enrichment scenario that the SN Ia rate steeply declines from $z = 0.37$ to $z = 0$ and/or a dominant number of SN Ia explosions occurred in higher redshifts.

This research was supported, in part, by a grant from the Hayakawa Satio Fund awarded by the Astronomical Society of Japan. YS is supported by Grant-in-Aid for JSPS Fellows. MK acknowledges support by the Grant-in-Aid for Scientific Research, No. 22740132.

Appendix 1. Spectral Analysis of Point Sources

As for point sources subtraction, we summarized position, photon index, and energy flux for point sources in table 4. In the case of `wavdetect` point sources, the fitting results to energy spectra are shown in figure 9. The detailed criteria of point source subtraction is summarized in section 3.2.

Appendix 2. Systematic Errors of Scaling Method

In the derivation of cumulative numbers, we assumed the uniform abundance profile of MS 1512.4+3647. We calculated the systematic error due to this assumption referring the average Fe abundance of several clusters in Matsushita et al. 2011. By comparing the amount of Fe integrated up to $0.3r_{200}$ between the case of uniform Fe abundance and the case of taking account of radial profile, the difference between two cases became roughly $\sim 30\%$. We took account this error into the derivation of cumulative numbers for MS 1512.4+3647. In the gas mass scaling of nearby clusters, the systematic error due to the

Table 4. Summary of point sources.

No.	α	δ	Γ	Flux*	Flux†	exclude‡
wawdetect						
1	228.551	36.538	$1.77^{+0.40}_{-0.37}$	$4.48^{+1.08}_{-1.08}$	$3.30^{+0.79}_{-0.80}$	○
2	228.470	36.546	1.7 (fix)	$2.05^{+1.26}_{-1.26}$	$1.60^{+0.98}_{-0.98}$	○
3	228.537	36.546	$1.56^{+0.58}_{-0.48}$	$3.65^{+1.17}_{-1.17}$	$3.17^{+1.01}_{-1.00}$	○
4	228.603	36.551	$1.28^{+0.62}_{-0.55}$	$2.30^{+1.25}_{-1.04}$	$2.40^{+1.31}_{-1.09}$	○
5	228.438	36.577	1.7 (fix)	$3.02^{+2.58}_{-2.58}$	$2.36^{+2.01}_{-2.32}$	○
6	228.596	36.580	$1.87^{+1.59}_{-1.06}$	$0.46^{+0.17}_{-0.21}$	$0.31^{+0.11}_{-0.14}$	—
7	228.594	36.582	1.7 (fix)	$0.33^{+0.14}_{-0.14}$	$0.26^{+0.11}_{-0.11}$	—
8	228.642	36.584	$1.86^{+0.30}_{-0.26}$	$3.97^{+0.59}_{-0.60}$	$2.72^{+0.41}_{-0.41}$	○
9	228.562	36.585	$1.56^{+0.46}_{-0.40}$	$0.91^{+0.25}_{-0.25}$	$0.79^{+0.22}_{-0.23}$	—
10	228.599	36.587	$2.99^{+0.22}_{-0.20}$	$1.86^{+0.20}_{-0.21}$	$0.41^{+0.04}_{-0.05}$	—
11	228.596	36.590	$1.29^{+0.80}_{-0.66}$	$0.52^{+0.28}_{-0.27}$	$0.54^{+0.29}_{-0.28}$	—
12	228.577	36.602	1.7 (fix)	$0.50^{+0.17}_{-0.17}$	$0.39^{+0.13}_{-0.13}$	—
13	228.617	36.605	$1.61^{+0.71}_{-0.71}$	$0.71^{+0.23}_{-0.25}$	$0.59^{+0.20}_{-0.21}$	—
14	228.580	36.614	$1.54^{+0.59}_{-0.49}$	$0.71^{+0.22}_{-0.23}$	$0.62^{+0.20}_{-0.20}$	—
15	228.618	36.629	$1.48^{+0.38}_{-0.33}$	$2.41^{+0.53}_{-0.54}$	$2.21^{+0.49}_{-0.50}$	○
16	228.613	36.634	1.7 (fix)	$0.33^{+0.17}_{-0.17}$	$0.26^{+0.13}_{-0.13}$	—
17	228.628	36.638	1.7 (fix)	$0.42^{+0.22}_{-0.23}$	$0.32^{+0.18}_{-0.17}$	—
18	228.587	36.647	$1.39^{+0.70}_{-0.62}$	$0.87^{+0.35}_{-0.34}$	$0.85^{+0.33}_{-0.34}$	—
19	228.607	36.648	1.7 (fix)	$0.47^{+0.24}_{-0.24}$	$0.36^{+0.19}_{-0.18}$	—
20	228.598	36.657	1.7 (fix)	$0.95^{+0.59}_{-0.60}$	$0.74^{+0.46}_{-0.46}$	—
21	228.656	36.678	$1.47^{+1.09}_{-0.71}$	$2.61^{+1.39}_{-1.32}$	$2.39^{+1.28}_{-1.21}$	○
22	228.592	36.680	1.7 (fix)	$0.59^{+0.37}_{-0.36}$	$0.46^{+0.29}_{-0.28}$	—
23	228.696	36.697	1.7 (fix)	$9.21^{+3.86}_{-3.36}$	$7.18^{+3.00}_{-3.01}$	○
24	228.490	36.704	1.7 (fix)	$2.87^{+1.86}_{-1.86}$	$2.24^{+1.45}_{-1.45}$	○
CSC						
25	228.450	36.548	1.7 (fix)	$1.44^{+0.38}_{-0.38}$	$1.16^{+0.32}_{-0.32}$	—
26	228.496	36.563	1.7 (fix)	$0.95^{+0.25}_{-0.25}$	$0.77^{+0.21}_{-0.21}$	—
27	228.400	36.568	1.7 (fix)	$1.55^{+0.66}_{-0.67}$	$1.25^{+0.54}_{-0.54}$	—
28	228.727	36.659	1.7 (fix)	$1.61^{+0.38}_{-0.38}$	$1.30^{+0.31}_{-0.31}$	—
29	228.799	36.675	1.7 (fix)	$2.50^{+0.80}_{-0.81}$	$2.02^{+0.66}_{-0.66}$	○
30	228.604	36.694	1.7 (fix)	$1.17^{+0.60}_{-0.60}$	$0.94^{+0.48}_{-0.48}$	—
31	228.685	36.710	1.7 (fix)	$11.60^{+0.86}_{-0.87}$	$9.37^{+0.74}_{-0.74}$	○
32	228.732	36.721	1.7 (fix)	$1.67^{+0.34}_{-0.33}$	$1.35^{+0.27}_{-0.27}$	—
33	228.724	36.732	1.7 (fix)	$1.18^{+0.29}_{-0.29}$	$0.95^{+0.23}_{-0.23}$	—
34	228.638	36.774	1.7 (fix)	$1.27^{+0.32}_{-0.33}$	$1.03^{+0.26}_{-0.26}$	—
2XMMi						
35	228.600	36.621	1.7 (fix)	8.73	7.53	○
36	228.487	36.665	1.7 (fix)	1.99	1.71	○
37	228.487	36.673	1.7 (fix)	4.43	3.80	○
38	228.543	36.696	1.7 (fix)	6.67	5.72	○

* 0.5–7.0 keV energy flux in units of 10^{-14} erg s $^{-1}$ cm $^{-2}$.† 2.0–10.0 keV energy flux in units of 10^{-14} erg s $^{-1}$ cm $^{-2}$.

‡ The mark of ○ means the excluded point source from the spectral analysis.

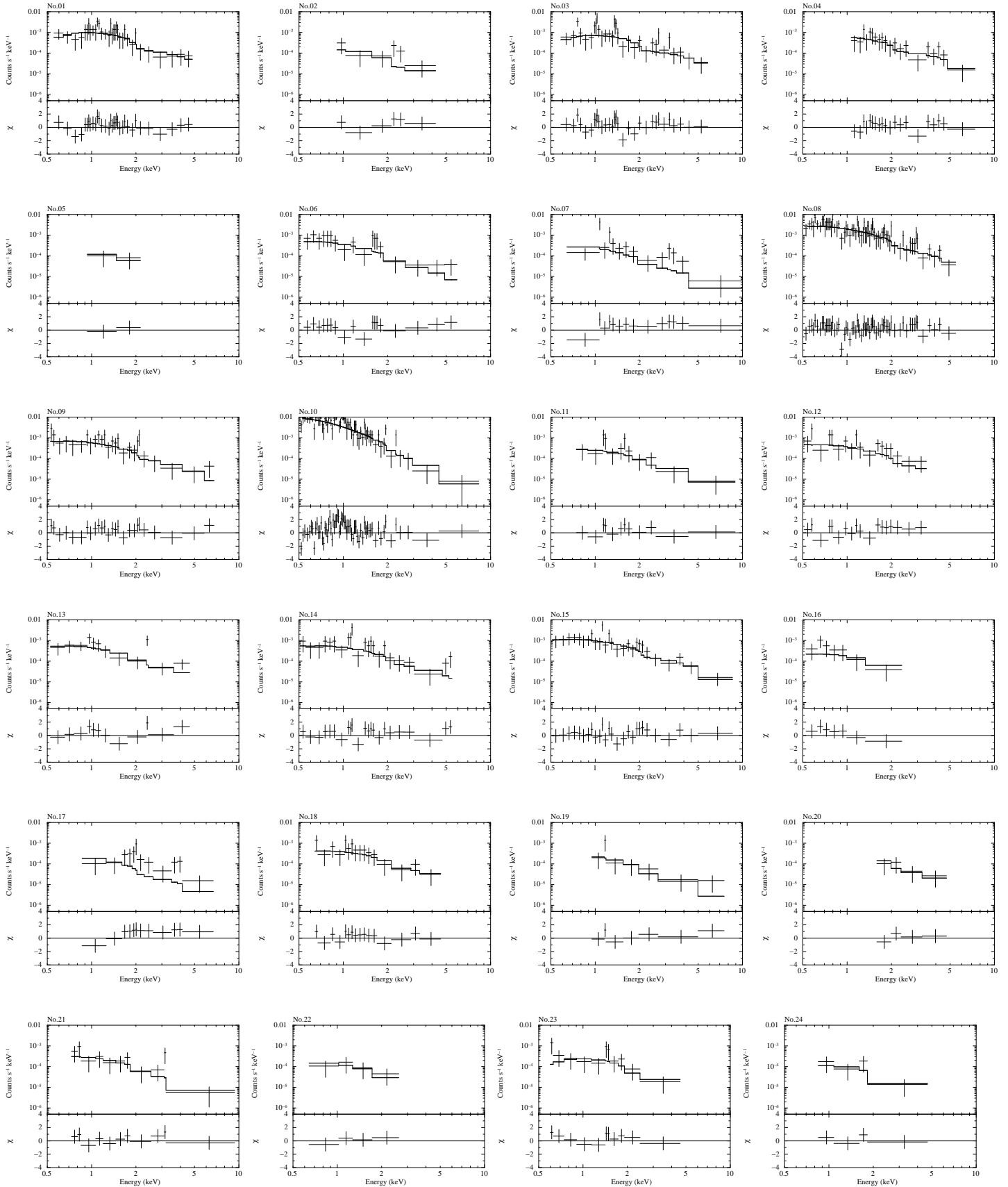


Fig. 9. ACIS spectra of detected point sources. The spectra of OBS1 and OBS2 are added.

accuracy of the abundance profile is considered. From several studies of spatially resolved nearby clusters, the amount of Fe integrated up to $0.3r_{200}$ have the statistical error of typically $\sim 20\%$ (e.g. Sato et al. 2007a). We took account this error into the gas mass scaling for the nearby clusters.

References

- Akamatsu, H., de Plaa, J., Kaastra, J., Ishisaki, Y., Ohashi, T., Kawaharada, M., & Nakazawa, K. 2012, PASJ, 64, 49
- Anders, E., & Grevesse, N. 1989, *Geochim. Cosmochim. Acta*, 53, 197
- Anderson, M. E., Bregman, J. N., Butler, S. C., & Mullis, C. R. 2009, *ApJ*, 698, 317
- Arnaud, M., Rothenflug, R., Boulade, O., Vigroux, L., & Vangioni-Flam, E. 1992, *A&A*, 254, 49
- Baldi, A., Etti, S., Molendi, S., Balestra, I., Gastaldello, F., & Tozzi, P. 2012, *A&A*, 537, 1
- Balestra, I., Tozzi, P., Etti, S., Rosati, P., Borgani, S., Mainieri, V., Norman, C., & Viola, M. 2007, *A&A*, 462, 429
- Bautz, M. W., et al. 1998, *Proc. SPIE*, 3444, 210
- Borgani, S., Fabjan, D., Tornatore, L., Schindler, S., Dolag, K., & Diaferio, A. 2008, *Space Sci. Rev.*, 134, 379
- De Grandi, S., Etti, S., Longhetti, M., & Molendi, S. 2004, *A&A*, 419, 7
- de Plaa, J., Werner, N., Bleeker, J. A. M., Vink, J., Kaastra, J. S., & Mendez, M. 2007, *A&A*, 465, 345
- Dickey, J. M., & Lockman, F. J. 1990, *ARA&A*, 28, 215
- Evans, I. N., et al. 2010, *ApJS*, 189, 37
- Ezawa, H., Fukazawa, Y., Makishima, K., Ohashi, T., Takahara, F., Xu, H., & Yamasaki, N. Y. 1997, *ApJ*, 490, L33
- Finoguenov, A., Arnaud, M., & David, L. P. 2001, *ApJ*, 555, 191
- Finoguenov, A., David, L. P., & Ponman, T. J. 2000, *ApJ*, 544, 188
- Fukazawa, Y., Makishima, K., Tamura, T., Ezawa, H., Xu, H., Ikebe, Y., Kikuchi, K., & Ohashi, T. 1998, *PASJ*, 50, 187
- Fukazawa, Y., Makishima, K., Tamura, T., Nakazawa, K., Ezawa, H., Ikebe, Y., Kikuchi, K., & Ohashi, T. 2000, *MNRAS*, 313, 21
- Freeman, P. E., Kashyap, V., Rosner, R., & Lamb, D. Q. 2002, *ApJS*, 138, 185
- Gal-Yam, A., Maoz, D., Sharon, K. 2002, *MNRAS*, 332, 37
- Garmire, G. P., Bautz, M. W., Ford, P. G., Nousek, J. A., & Ricker, G. R. 2003, *Proc. SPIE*, 4851, 28
- Gunn, J. E. & Gott, J. R. 1972, *ApJ*, 176, 1
- Hayashida, K. 1989, PhD thesis, The University of Tokyo
- Henry, J. P., Evrard, A. E., Hoekstra, H., Babul, A., & Mahdavi, A. 2009, *ApJ*, 691, 1307
- Hoshino, A., et al. 2010, *PASJ*, 62, 371
- Ishisaki, Y., et al. 2007, *PASJ*, 59, S113
- Iwamoto, K., Brachwitz, F., Nomoto, K., Kishimoto, N., Umeda, H., Hix, W. R., & Thielemann, F.-K. 1999, *ApJS*, 125, 439
- King, I. R. 1962, *AJ*, 67, 471
- Komiyama, M., Sato, K., Nagino, R., Ohashi, T., & Matsushita, K. 2009, *PASJ*, 61, S337
- Koyama, K., et al. 2007, *PASJ*, 59, S23
- Kushino, A., Ishisaki, Y., Morita, U., Yamasaki, N. Y., Ishida, M., Ohashi, T., & Ueda, Y. 2002, *PASJ*, 54, 327
- Lodders, K. 2003, *ApJ*, 591, 1220
- Loewenstein, M. 2006, *ApJ*, 648, 230
- Lumb, D. H., Warwick, R. S., Page, M., & De Luca, A. 2002, *A&A*, 389, 93
- Mannucci, F., Della Valle, M., & Panagia, N. 2006, *MNRAS*, 370, 773
- Maoz, D., Mannucci, F., & Brandt, T. D. 2012, *MNRAS*, 426, 3282
- Mathews, W. G., Baker, J. C. 1971, *ApJ*, 170, 241
- Matsushita, K. 2011, *A&A*, 527, A134
- Matsushita, K., et al. 2007, *PASJ*, 59, S327
- Maughan, B. J., Jones, C., Forman, W., & Van Speybroeck, L. 2008, *ApJS*, 174, 117
- Mitsuda, K., et al. 2007, *PASJ*, 59, S1
- Nakazawa, K., et al. 2009, *PASJ*, 61, 339
- Nomoto, K., Tominaga, N., Umeda, H., Kobayashi, C., & Maeda, K. 2006, *Nucl. Phys. A*, 777, 424
- Ota, N. 2000, PhD thesis, Univ. of Tokyo
- Renzini, A., Ciotti, L., D'Ercole, A., & Pellegrini, S. 1993, *ApJ*, 419, 52
- Sakuma, E., Ota, N., Sato, K., Sato, T., & Matsushita, K. 2011, *PASJ*, 63, S979
- Sato, K., et al. 2007a, *PASJ*, 59, 299
- Sato, K., Kawaharada, M., Nakazawa, K., Matsushita, K., Ishisaki, Y., Yamasaki, N. Y., & Ohashi, T. 2010, *PASJ*, 62, 1445
- Sato, K., Matsushita, K., & Gastaldello, F. 2009b, *PASJ*, 61, S365
- Sato, K., Matsushita, K., Ishisaki, Y., Yamasaki, N. Y., Ishida, M., & Ohashi, T. 2009a, *PASJ*, 61, S353
- Sato, K., Matsushita, K., Ishisaki, Y., Yamasaki, N. Y., Ishida, M., Sasaki, S., & Ohashi, T. 2008, *PASJ*, 60, S333
- Sato, K., Tokoi, K., Matsushita, K., Ishisaki, Y., Yamasaki, N. Y., Ishida, M., & Ohashi, T. 2007b, *ApJ*, 667, L41
- Serlemitsos, P. J., et al. 2007, *PASJ*, 59, S9
- Smith, R. K., Brickhouse, N. S., Liedahl, D. A., & Raymond, J. C. 2001, *ApJ*, 556, L91
- Snowden, S. L., Mushotzky, R. F., Kuntz, K. D., & Davis, D. S. 2008, *A&A*, 478, 615
- Stoeckle, J. T., et al. 1991, *ApJS*, 76, 813
- Strolger, L.-G., et al. 2004, *ApJ*, 613, 200
- Tamura, T., et al. 2009, *ApJ*, 705, L62
- Tawa, N., Hayashida, K., Nagai, M., Nakamoto, H., & Tsunemi, H. 2008, *PASJ*, 60, S11
- Tokoi, K., et al. 2008, *PASJ*, 60, S317
- Tornatore, L., Borgani, S., Dolag, K., & Matteucci, F. 2007, *MNRAS*, 382, 1050
- Watson, M. G., et al. 2009, *A&A*, 493, 339
- Weisskopf, M. C., Brinkman, B., Canizares, C., Garmire, G., Murray, S., & Van Speybroeck, L. P. 2002, *PASP*, 114, 1
- Weisskopf, M. C., Tananbaum, H. D., Van Speybroeck, L. P., & O'Dell, S. L. 2000, *Proc. SPIE*, 4012, 2
- Yoshino, T., et al. 2009, *PASJ*, 61, 805